AN IN-SITU HE IMPLANTER APPROACH TO IRRADIATIONS WITH CONTROLLED HE/DPA RATIOS AT FUSION RELEVANT CONDITIONS—T. Yamamoto, G. R. Odette (University of California, Santa Barbara), and L. R. Greenwood (Pacific Northwest National Laboratory)

OBJECTIVE

This research is aimed at designing and implementing a novel method for in-situ He implantation in mixed spectrum reactor irradiations at controlled and fusion relevant He/dpa ratios and dpa rates. The implantation of He from ^{6}Li(n,α) reactions into and through vanadium alloy substrate insulator coatings in fusion neutron spectra is also examined.

SUMMARY

The design and implementation of a novel in-situ He-implanter technique, utilizing the ^{59}Ni(n,α) reaction, to characterize the effect of the He/dpa ratio on microstructural evolution and changes in the flow properties for fusion relevant alloys and conditions (dpa, dpa rate, and temperature) is described. Irradiations (JP-26, JP27, and JP28/29) in the peripheral target (PTP) positions in the High Flux Isotope reactor (HFIR) result in α-implantation from thin layers of NiAl into adjacent iron based alloys, yielding a region of uniform He concentration of 5 to 50 appm He/dpa to a depth of 5 to 8 μm. Electron beam co-deposition of Al and Ni was used to produce 1 to 5 μm thick NiAl coatings on TEM discs. The NiAl coatings were characterized by a number of techniques. The He-implantation technique was applied to three types of materials: cold worked and annealed unalloyed Fe, ≈ 8Cr tempered martensitic steels (TMS) and nano-dispersion strengthened ferritic alloys (NFAs). Other approaches to, and applications of, in-situ He implantation are also described. Our primary objective is to assess He transport, fate and consequences, as well as He management by trapping at nanoscale precipitate interfaces. We also examine He implantation from Li in fusion neutron spectra into and through insulator coatings on vanadium alloy substrates.

Introduction

Predicting and mitigating the effects of combinations of large levels of transmutation product He and displacement damage (dpa) produced by high energy neutrons on the mechanical properties of structural materials is one of the key challenges in the development of fusion energy. Indeed there the fundamental overriding questions about He-dpa synergisms include:

> What is the transport and fate of He and displacement damage defects and the consequential effects on microstructural evolutions and mechanical property changes?
>
> What are the basic interacting mechanisms controlling He and defect transport, fate, and consequences?
>
> How is He and defect transport, fate, and consequences influenced by the combination of the starting microstructure (and microchemistry) of the material and irradiation variables (dpa rate, He/dpa ratio, temperature, and applied stress) and variable history?
>
> How can the detrimental effects of He-dpa synergisms be mitigated and managed, primarily by proper design of the materials starting microstructure?

Indeed, understanding the effects of He-dpa synergisms on microstructural evolutions and property changes under fusion relevant conditions (He/dpa ≈ 10 appm/dpa, 10^{-6} dpa/s) is <u>the</u> primary motivation for proposals to construct a high-energy fusion neutron source, such as the IFMIF. However, in the meantime, it will be necessary to utilize fission reactor and dual ion irradiations to study He-dpa synergisms. Dual ion irradiations are useful to explore mechanisms, but they do not simulate fusion conditions because of their highly accelerated dpa rates and other confounding factors, such as the

proximity of free surface sinks. To date, most fission reactor studies of He-dpa synergisms have utilized ^{59}Ni and ^{10}B (n,α) 'alloying element' reactions to produce high levels of He. However, with the exception of austenitic stainless steels, neither Ni nor B constitutes a normal alloying element in candidate fusion structural material systems (≈ 8Cr tempered martensitic steels, nano-dispersion strengthened ferritic alloys, solid solution vanadium alloys, and SiC/SiC ceramic composites). Thus, while artificially adding Ni or B, combined with isotopic and/or spectral tailoring, is very useful, these techniques cannot be considered simulations either, since doping introduces a significant number of confounding factors. It is also noted that spallation proton irradiations produce ultra-high levels of He at rates of ≈ 80 to 150 appm/dpa.

In-situ He implantation in fission reactors is an alternative and very attractive approach to assessing the effects of He-dpa synergisms that avoids most of the confounding effects of doping. The basic idea is to use an implanter foil to inject high-energy α-particles from (n,α) reactions into an adjacent sample undergoing displacement damage. Implanting He using the decay of an α-emitting radioactive isotope adjacent to the target specimen was first proposed in the late 1970s to early 1980s [1,2]. However, the isotope decay technique produces few dpa and, thus, a very high He/dpa ratio. Different variants of a He implanter foil technique utilizing (n,α) reactions from triple fission [3] (to exploit the high α-energy) and ^{59}Ni-type isotope reactions reaction [3,4] to produce fusion relevant He/dpa ratios in virtually any material of choice were first proposed in the mid-to-late 1980s. The triple fission technique was applied a tensile specimen of a ferritic steel [5]. However, this experiment was not completely successful due to difficulties in controlling temperature increases arising from heat generated by the fission reaction, as well as in obtaining the desired He/dpa ratio.

An implanter approach based on the ^{59}Ni(n_{th},α) reaction is much simpler to implement. However, this idea lay dormant for many years, but was resurrected by our group at UCSB in the early part of planning for a series of HFIR experiments that form the core of the US-JAERI fusion materials collaboration. We decided that a thin μm-scale Ni containing coating layer on TEM discs would serve as a good implanter foil. In this case, He is implanted uniformly over ≈ 5 to 8 μm layer. This is sufficiently thick for low load Vickers micro-hardness and nano-hardness measurements, as well as for extensive microstructural characterization. Hence, the objective of the initial phase of this research was to design, develop, and implement a technique to deposit and characterize Ni containing implanter foils on TEM discs to be included in coated-uncoated pairs in the HFIR-PTP irradiations, with nominal peak target doses of 10, 25, and 60 dpa at irradiation temperatures of 300, 400, and 500°C.

Implanter Foil Design Concepts

There are three basic approaches to implanter *foil* design. Here we will refer to *thin* and *thick*, specifically meaning a specimen (t_s) or implanter foil (t_f) thickness that is less than or greater than the corresponding α-particle range, respectively. Thin foils produce uniform implantation at a selected, implanter foil thickness-dependent He/dpa ratio. Thick implanter foils on one side of a thick specimen produce linear concentration profiles, with the maximum concentration of He at the specimen surface. Thick implanter foils on both sides of a thin specimen also produce a uniform concentration profile at the maximum concentration of He. In this section, the conceptual design of a thin implanter foil is first summarized, followed by a description of the actual fabrication and characterization of NiAl coatings on TEM discs to attain controlled fusion relevant He/dpa ratios in the JP26 to JP28/29 experiments.

<u>He Implantation Profiles</u>

The implanter foil contain an isotope with a large (n,α) reaction cross section, such as ^{59}Ni, ^{10}B, ^{6}Li, producing an α-particle with characteristic energy and corresponding range in the foil and sample of R_f and R_s, respectively. Figure 1a shows thick specimen, thick implanter foil configuration. The α-particles emitted from the foil under neutron irradiation are deposited in the specimen up to the depth of R_s. All calculations in this section assume the area (y, z) dimensions of the implanter foil-specimen are much larger than R_f,, hence, edge effects can be neglected. For simplicity, we first assume $R_f = R_s = R$ and

ignore α-particle straggling. The He concentration, C_{He}, at a depth x ($x < R$) in the specimen is proportional to the area fraction, $f(x)$, of the spherical shell in the implanter foil of radius, R, centered on x, as shown in Fig. 1b. The $f(x)$ is given by:

$$f(x) = \int_0^{\theta_{max}} 2\pi R \sin\theta \bullet R d\theta \Big/ 4\pi R^2 = \frac{1}{2}\left(1 - \frac{x}{R}\right) \tag{1}$$

Here θ is the angle between the radial vector R and the normal to the specimen surface and θ_{max} occurs at the implanter foil/specimen boundary. The resulting He concentration profile is linear, with $f(x)$ decreasing from 1/2 at x = 0 to 0 at $x = R_s$. Difference in the implanter foil versus specimen α-particle ranges, R_f and R_s, are accounted for by a range ratio factor of R_f/R_s, and $C_{He}(x)$ is given by:

$$C_{He}(x) = \frac{C_f}{2}\frac{R_f}{R_s}\left(1 - \frac{x}{R_s}\right) \tag{2}$$

Here C_f is the volumetric concentration of He in the implanter foil which is the same as the bulk concentration for a given implanter foil composition and neutron dose. The corresponding molar (or atomic) concentration c_f must be adjusted by multiplying C_f by the ratio of the foil/specimen atomic densities (N), N_f/N_s.

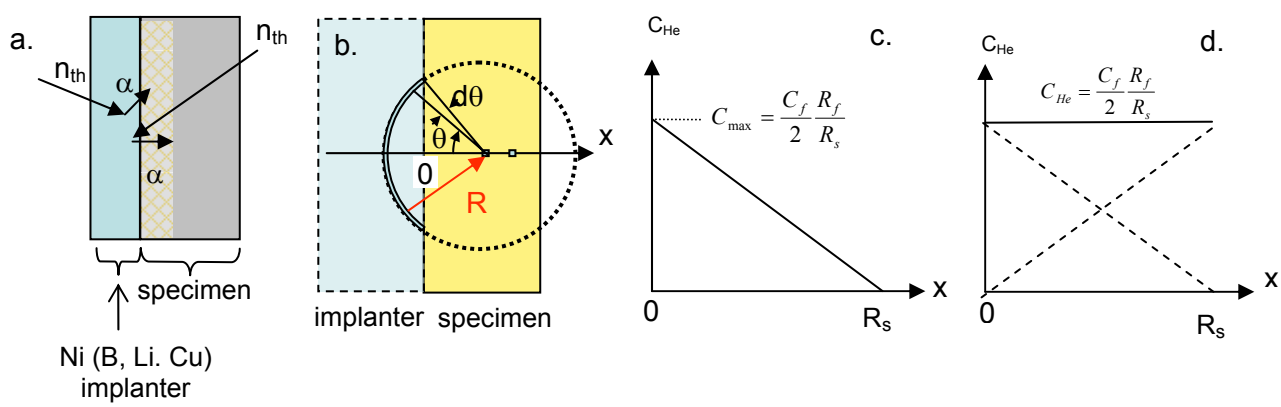

Fig. 1. Schematic illustration of a) a thick implanter foil; b) the implanter source volume for He deposited at a depth x in the specimen; c) the He concentration profile for thick foil implantations from one side of a thick specimen; and d) the uniform He concentration profile for thick foil implantations from both sides of a thin specimen (in this case with $t_s = 2R_s$).

The gradient in the He concentration may be acceptable, or even advantageous, in some cases. However, in others a uniform He distribution is preferable. As noted above regions with uniform concentrations can be obtained using thin specimens implanted from both sides. However there are practical difficulties in fabricating such thin specimens. Fortunately, as illustrated in Fig. 2a, a uniform distribution of He near the surface of a thick specimen can also be obtained by using thin implanter foils, with $t_f << R$. The He profile for a thin implanter can be determined by simply superimposing linear profiles from various depths in the foil, after subtracting off the *missing* contributions from the (n,α) reactions further from the interface. For $R_f = R_s = R$, the result is a uniform region of He concentration of $C_{He}(x) = [C_f/2][t_f/R]$ up to a maximum $x_m = R - t_f$. At larger $x > R - t_f$ the $C_{He}(x)$ decreases from $[C_f/2][t_f/R]$ to 0 at x = R. In the case where $R_f \neq R_s$ the $x_m = R_f(1 - t_f/R_s)$. Thus,

$$C_{He}(x) = \begin{cases} \dfrac{C_f}{2}\dfrac{t_f}{R_s} & (0 \le x \le x_m) \\ \dfrac{C_f}{2}\dfrac{R_f}{R_s}\left(1 - \dfrac{x}{R_s}\right) & (x_m < x < R_s) \end{cases} \tag{3}$$

As illustrated in Fig. 2b, implantation from thin foils on both sides of the specimen with $t_s = 2R_s - x_m$ result in a uniform helium concentration.

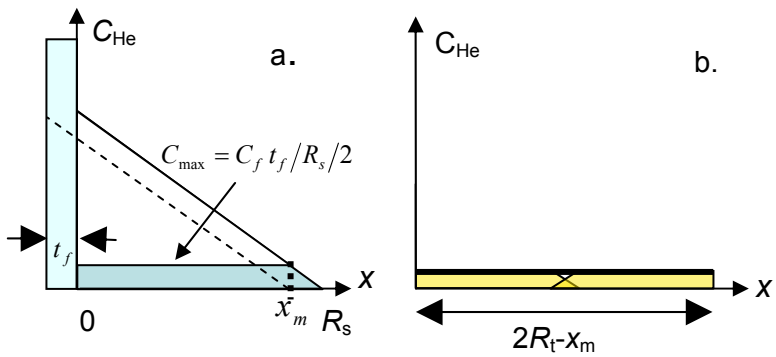

Fig. 2. Schematic illustration of the $C_{He}(x)$ for thin implanter foils on: a) a single side; b) both sides. The key conclusions from this analysis are:

1. Various He profiles in a specimen can be produced with combinations of one or two-sided thick or thin implanter foil and specimen combinations.

2. Uniform helium concentrations can be produced over useful regions of a specimen by thin foil implantation from one side.

3. The concentration of He in a specimen can be controlled by both the thickness and composition (coupled with the neutron spectrum) of a thin implanter foil. Thus it is possible to control (dial-in) the corresponding He/dpa ratio over a wide range of values.

4. Thin foil implantation from two sides of a thin specimen roughly doubles the size of the region with a uniform He concentration.

5. In principle the implanter technique is optimized by using (n,α) reactions with the highest α-particle energy possible. For example, the triple ^{235}U fission produces α-particles with a typical energy of ≈ 16 MeV corresponding to a range of ≈ 60 μm in Fe and a maximum thin specimen thickness up to ≈ 60 μm [3]. This dimension is sufficient for specialized tensile specimen tests, possibly even in the creep regime. Further, while the dimensions are far too small for measuring fast fracture properties, they may be sufficient to measure fast fracture related processes and mechanisms, such as weakening of grain boundaries due to He accumulation.

While the implanter foil concept is not new [3,4] the opportunities that it presents, perhaps aptly described as a micro IFMIF, have been neglected for far too long. Thus, in the following section, we describe the detailed design and first implementation of the in-situ implanter technique as part of the JP26 to 29 experiments in HFIR.

He Implanter Foil Design for Iron Based Alloys Irradiated in the HFIR PTP JP26 to 28/29 Experiments

The ^{59}Ni isotope is the obvious leading candidate (n,α) reaction source, yielding a 4.79 MeV α-particle. Since ^{59}Ni is radioactive, with a half life of $t_{1/2}$ = 7.5x10^4 y, the simplest approach is to breed it in-situ based on the reaction sequence ^{58}Ni(n, γ)^{59}Ni(n,α). The time-dependent concentration of ^{59}Ni(n,α), hence, the generation rate of He in the implanter foil, depends on the pertinent spectral averaged ^{58}Ni(n_{th}, γ), ^{59}Ni (n_{th},α), and total ^{59}Ni n-absorption ^{59}Ni (n_{th},tot.) cross sections. The total dpa is also determined by the corresponding spectral averaged dpa cross section. The pertinent cross sections were used to compute He concentration, c_{He} (appm), for pure Ni versus dpa for irradiations in the HFIR PTP spectrum, shown as the solid line in Fig. 3 [6]. The open squares are measurements of c_{He}. Agreement between experiment and the prediction is very good at low dpa, but deviations at higher dose indicate the presence of another reaction source for He. Nevertheless, our implanter foil design is based on the predictions shown in the solid line in Fig. 3.

We chose to use the intermetallic compound NiAl rather than pure Ni for a number of reasons including: a) NiAl is believed to be more stable under irradiation than pure Ni, since the latter would have the tendency to swell; b) NiAl has a coefficient of thermal expansion that is similar to that of ferritic steels; c) it is relatively easy to co-deposit Ni and Al wide over the stable composition range of single phase NiAl, from 46 to 59 at %. Table 1 lists the densities of NiAl and ferritic steels and the corresponding 4.76 MeV α-particle ranges used in the implanter foil design. The α-particle ranges were calculated using TRIM 2002 code as the average for of 10000 4.76 MeV He ions.

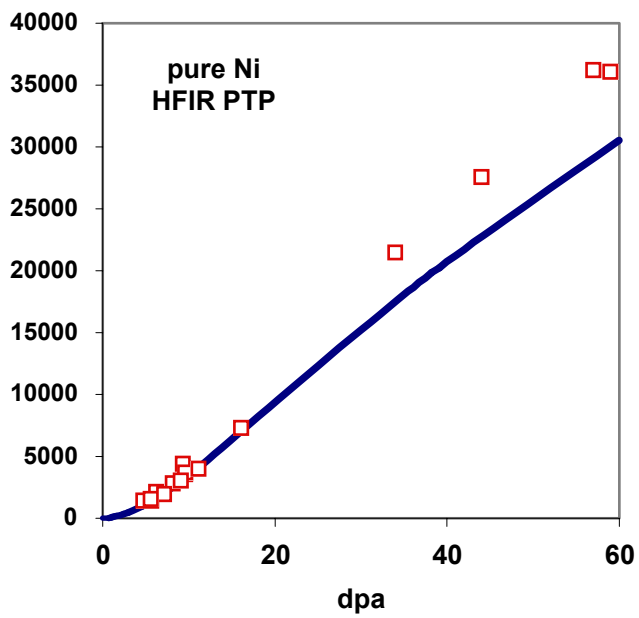

Fig. 3. He concentration versus dpa in pure Ni irradiated in HFIR PTP target capsule.

Table 1. Parameters used for the NiAl implanter foil design

Density of NiAl	5.90 g/cm^3
Density of 8Cr-2W steel	7.9 g/cm^3
Energy of α-particle from ^{59}Ni(n,α)	4.76 MeV
Range in NiAl	11.5 μm
Range in 8Cr-2W steel	9.1 μm
Nominal He/dpa ratio (for 5 dpa)	5, 10, 20*
Nominal He/dpa ratio for 25 & 60 dpa	10, 20, 50

Figure 4 shows the He concentration profiles in ferritic steel specimens for NiAl implanter foils with t_f = 1, 2, and 4 μm for low (4.3 dpa) and high (60 dpa) dose conditions, corresponding to target exposures for the JP-26 and JP-28/29 capsules, respectively. Due to the dose transient to 'burn-in' ^{59}Ni to a quasi steady-state concentration, producing an approximately constant He generation rate (see Fig. 3), the He/dpa ratio roughly doubles in going from the lowest to highest dose. Thus implanter foil designs targeting a specified He/dpa ratio must consider the intended dpa dose. There is also a direct trade-off between the implanter foil thickness, or the corresponding region of uniform He composition in the specimen and the maximum He/dpa ratio that can be achieved. Nevertheless, even at the lowest dose irradiation, an average He/dpa ratio of 20 appm He/ dpa can be attained over an ≈ 6 μm thick specimen region. Implanter foil thicknesses of 1, 2, and 4 μm yield He/dpa ratios of ≈ 5, 10, and 20 appm He/ dpa at the target dose of 4.3 dpa for the JP26 capsule. However, rather than trying to make thinner coatings, which are more difficult to characterize, similar implanter foil thicknesses were used in the JP27 experiment, with a target dose of 25 dpa, leading to He/dpa ratios of ≈ 10, 20, and 50 appm He/dpa. The foil thicknesses were slightly reduced in the JP28/29 experiment, with a target dose of 60 dpa, to maintain similar He/dpa ratios of 10, 20, and 50 appm He/dpa.

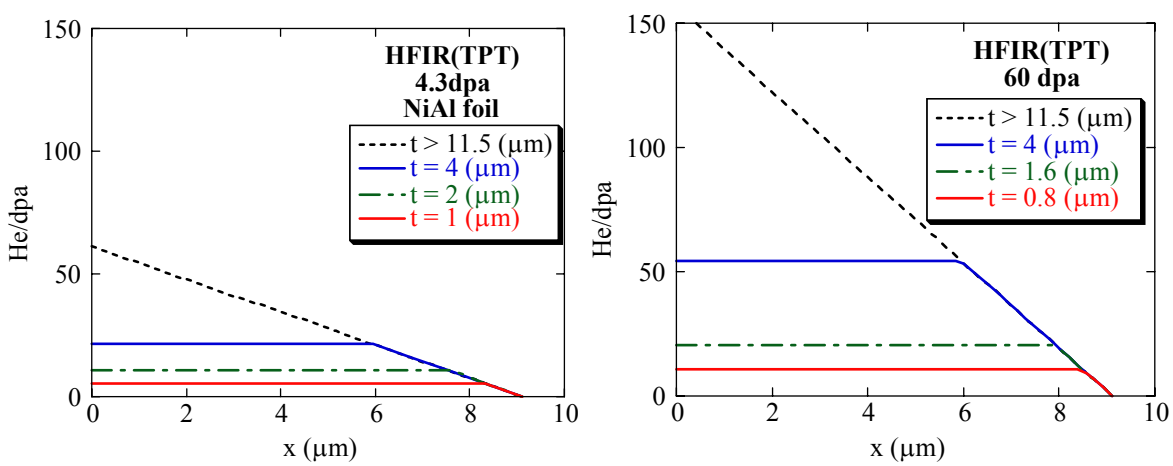

Fig. 4. He concentration profiles in ferritic steel specimens for low (4.3 dpa) and high (60 dpa) dose conditions corresponding to targets for the JP-26 and JP-28/29 capsules, respectively, for NiAl implanter foils with t_f = 1, 2, and 4 μm.

Implanter Foil Fabrication and Characterization

Thin 0.8 to 5 μm NiAl implanter foils were deposited on TEM disc specimens. The sequence of steps in the overall deposition and coating characterization process is schematically summarized in Fig. 5. First TEM disc surfaces were polished on both sides. The deposition side was finished to 0.05 μm alumina to ensure the dense growth of the NiAl deposition layer, while the other side was finished to 1200 grit paper to maintain good heat transfer for substrate temperature control during deposition. Ni and Al were co-deposited using electron beam (EB) physical vapor deposition (PVD) system. The deposition rates of each element were independently monitored with a calibrated crystal oscillator mass monitor. The EB currents were adjusted and controlled to maintain the desired 1/1 Ni/Al atomic ratio in the deposit. The TEM disc substrate temperature was held at 500 ºC during deposition. The co-deposited film was grown at a typical rate of ≈ 1 um/h.

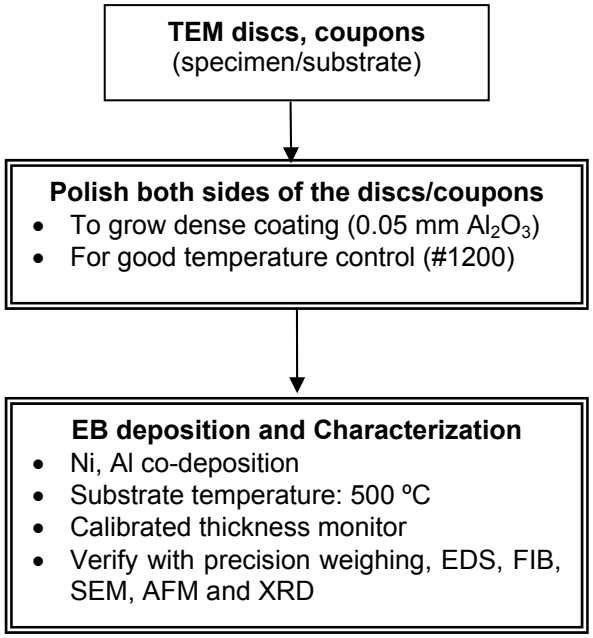

Fig. 5. A schematic summary of the processing and characterization steps used in the preparation of implanter foils deposited on TEM disc samples.

Careful characterization of the implanter foil coating was an extremely important part of this work, especially during the stage of developing and calibrating the deposition procedure. The characterization included the following procedures.

The primary technique to characterize the effective thickness of the coatings was based on pre- and post-deposition precision weighing of the thin substrate monitors, as well as essentially all of the TEM discs. The overall thickness uncertainties of the weighing technique is estimated to be ≈ ±0.1 μm.

Cross-sections of the discs-coatings system were examined in the SEM to characterize the adherence of the coating and any defects present. The coatings were generally found to be well bonded and defect free.

The coatings were also selectively micro-machined and imaged in the FIB for similar reasons.

SEM EDX spectra measurements were used to measure the composition of the deposits, which generally ranged from 48 to 55 at % Ni. Calibration of the Fe signal as a function of the coating

thickness was also used to help verify the coating thickness. SEM EDX was used to examine essentially 100% of the coated TEM discs used in the irradiations.

XRD was selectively used to verify the presence of a single NiAl phase.

AFM was selectively used to characterize the roughness of the coating layer.

Figure 6 shows examples of the film characterization procedures. The FIB cross sectioning showed that dense implanter layer coating had grown continuously from the substrate surface to the target thickness. XRD showed that the deposited film consists of single-phase NiAl. The surface roughness measured by AFM was typically ≤ 0.04 μm, reflecting the substrate roughness. Overall, the roughness and coating thickness variations are expected to contribute spatial differences in the He concentration of less than 4 %. Along with crystallographic information from XRD, the EDX analyses confirmed that the Ni content was within the range of NiAl phase.

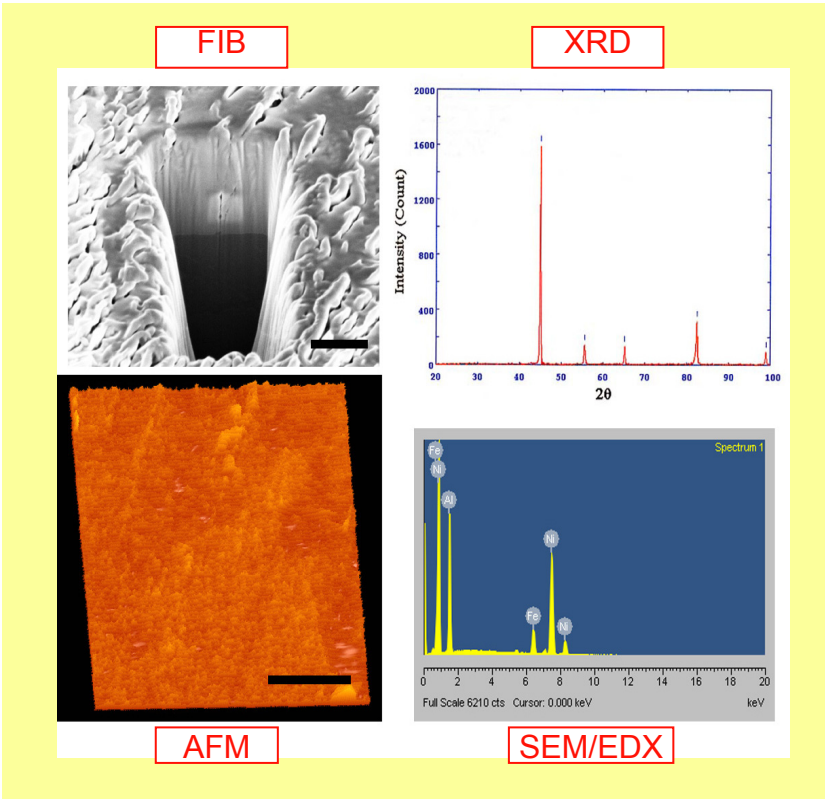

Fig. 6. Examples of the various techniques used to characterize the implanter foil coatings (FIB, XRD, AFM, and SEM/EDX).

In the case of the JP-26 and 27 capsules, the discs were laser engraved at PNNL with a specimen and irradiation capsule codes on the outer periphery of uncoated side after coating with the NiAl implanter foil. For JP-28/29 capsule the discs were engraved before coating. All discs were subsequently optically inspected to verify that they remained damage free. A total of approximately 400 coated discs were fabricated and characterized as described above, and a subset of about 300 of them that best achieved a high quality implanter foil coating were selected for subsequent irradiations. The coated discs were paired with highly polished uncoated discs that experience similar He/dpa ratios.

Irradiation Experiments and Post-Irradiation Characterization Studies

Specimen Matrix and Irradiations

As noted previously, the He-implantation technique has been applied to three types of materials: cold worked and annealed unalloyed Fe, ≈ 8Cr tempered martensitic steels (TMS) and nano-dispersion strengthened ferritic alloys (NFA). The coated and paired uncoated TEM discs have been included in the JP26, JP27, and JP28/29 experiments that have been (JP26), or are being (JP27 and JP28/29), irradiated to nominal doses of 4 to 60 dpa, with He/dpa ratios of 5 to 50 appm, at irradiation temperatures of 300, 400, and 500°C. Table 2 summarizes the details of the total ≈ 540 He injected TEM discs that are included in these experiments. Of course, normal TEM specimens of all the materials are included in the matrix to provide a low He/dpa (< 1 app He/dpa) baseline for the effects of higher He. Further, the matrix includes some Ni-doped model alloys as an alternative means of introducing He. Note that the experiments are closely integrated with modeling studies of the transport and fate of He, the effects of the He/dpa ratio on microstructural evolution and He management in NFA, exploiting gas trapping at the interfaces of non-equilibrium, nano-scale precipitates [7].

Post Irradiation Characterization Studies

Various types of TEM techniques will be used as the primary tool for post-irradiation characterization studies, with the 5-8 μm region of the specimen with a uniform concentration of He made readily accessible by a variety of well-developed sample preparation techniques, including back thinning, cross-sectioning, and FIBing. The TEM studies will focus on: a) the fate of helium; b) the effect of the He/dpa ratio on the overall microstructural evolution; c) the effects of synergistic interactions between the He/dpa ratio and other irradiation variables (dpa, temperature) and metallurgical variables (the starting microstructure and microchemistry) on He fate and microstructural evolution; and c) the ability of nano-scale precipitates and dislocations to trap and disperse (manage) He in fine-scale bubbles. It is notable that the enormous range of microstructures covered by these three classes of materials not only provides an unprecedented opportunity to better understand key mechanisms and processes, but will also yield a database to guide the design of new and improved alloy systems.

For example, the behavior and effects of He in the cold-worked and annealed Fe will provide clear, single-variable-type insight on the effects of dislocation structures on the transport and fate of He. The NFA in the specimen matrix include a series of model materials produced by UCSB (the U14-series) and ORNL (the O14 alloy). The U14YWT and U14WT variants include HIPing at 850, 1000, and 1150°C resulting in a wide range of fine scale precipitate structures, with large differences in their sizes, number densities (hence, sink strengths), and basic structures (hence, different interface characteristics) ranging from non-equilibrium coherent Y-Ti-O clusters to semi-coherent, pyroclore-type, and other oxide phases. The specimen matrix also includes MA957, the Japanese 12WYT, and the ODS PM2000 alloys. Note, depending on the alloy and processing path, the NFA also represent a wide range of dislocation and grain structures as well. The TMS in the matrix include 3 variants of F82H, including one with 20% cold work and Eurofer97. The basic microstructure of the TMS consists of: a) μm-scale laths arranged in small ≤ 10 μm lath packets bundles that are contained in larger 20 to 80 μm prior austenite grains; b) medium-to-coarse scale Cr-rich carbides; and, c) medium-to-high (the cold-worked alloy) dislocation densities. The TMS microstructures also provide many trapping sites for He, but recent evidence suggests that even so, He accumulation prior austenite grain boundaries may lead to a severe non-hardening embrittlement and intergranular fast fracture at lower irradiation temperatures (≤ ≈ 350°C), and that these microstructures are unstable at higher irradiation temperatures (> 450°C) [8,9]. Other potential characterization techniques include x-ray scattering, positron annihilation spectroscopy, and He desorption spectroscopy.

Sectioned discs will also be used for both conventional and advanced micro/nano-hardness measurements that will provide a direct, side-by-side comparison of the effect, if any, of the He/dpa ratio on the irradiated flow properties. Future studies based on similar and alternative implantation methods and specimen geometries could be used to study the amount and consequences of helium accumulation

Table 2. The implanted TEM matrix in the JP26, JP27, and JP28/29 capsules

T_i = 300 ºC	dpa	JP-26			JP-27			JP-28/29		
	He/dpa (appm)	4.3			11			25		
	NiAl thickness (μm)	5	11	21	10	20	50	10	21	52
Material		1	2	4	1	2	5	0.8	1.6	4
Fe		1	2	1	1	2	1	1	2	1
Fe+20%CW		2	2	2	2	2	2	2	2	2
F82H IEA		2	2	2	2	2	2	2	2	2
F82H-mod.3		2	2	2	2	2	2	2	3	2
F82H-mod.3+20%CW		2	2	2	2	2	2	2	2	2
Eurofer 97		2	2	2	2	2	2	2	2	2
U14YWT850				3			3		1	3
U14YWT1150				3			3			3
U14YW1150				3			3			3
O14YWT850				3			3			3
U14WT1000				2						
U14WT1150							2			2
MA957 (US)				2			2	1		2
MA957 (F)				2			2			2
12YWT		2	2	2	1		2	1	2	2
PM2000				2	1	2	2			2
Total		13	14	33	13	14	33	13	16	33

T_i = 400 ºC	dpa	JP-26			JP-27			JP-28/29		
	He/dpa (appm)	4.3			11			54		
	NiAl thickness (μm)	5	11	21	10	20	50	11	22	55
Material		1	2	4	1	2	5	0.8	1.6	4
Fe		1	2	1	2	1	1	1	2	1
Fe+20%CW		2	2	2	2	2	2	2	2	2
F82H IEA		2	2	2	2	2	2	2	2	2
F82H-mod.3		2	2	2	2	3	2	2	2	2
F82H-mod.3+20%CW		2	2	2	2	2	2	2	2	2
Eurofer 97		2	2	2	2	2	2	2	2	2
U14YWT850				3			3		1	3
U14YWT1150				3			3			3
U14YW1150				3			3			3
O14YWT850				3			3			3
U14WT1000				2						
U14WT1150							2			2
MA957 (US)				2			2	1		2
MA957 (F)				2			2		1	2
12YWT		2	2	2		1	1	2	2	2
PM2000				2	2		2			2
Total		13	14	33	14	13	32	14	16	33

Table 2. The implanted TEM matrix in the JP26, JP27, and JP28/29 capsules (continued)

T_i = 500 °C	dpa	JP-26			JP-27			JP-28/29		
	He/dpa (appm)	10			25			60		
	NiAl thickness (μm)	9	19	38	13	25	65	11	22	55
Material		1	2	4	1	2	5	0.8	1.6	4
Fe		1	2	1	2	1	1	1	2	1
Fe+20%CW		2	2	2	2	2	2	2	2	2
F82H IEA		2	2	2	2	2	2	2	2	2
F82H-mod.3		2	2	2	2	2	2	2	2	2
F82H-mod.3+20%CW		2	2	2	2	2	2	2	2	2
Eurofer 97		2	2	2	2	2	2	2	3	2
U14YWT850				3			3		1	3
U14YWT1150				3			3			3
U14YW1150				3			3			3
O14YWT850				3			3			3
U14WT1000				2						
U14WT1150							2			2
MA957 (US)				2			2	1		2
MA957 (F)				2			2			2
12YWT		2	2	2		1	2	2	2	2
PM2000				2	2	1	2			2
Total		13	14	33	14	13	33	14	16	33

on grain boundaries, including gas release studies and assessment of the effects of He on grain boundary decohesion and fast fracture at low temperatures and creep rupture cavitation processes at high temperatures. This may be possible, even in the case of thin implanted layers, by using disc bulge/ball punch type tests. Further, the effects of applied stress on the transport and fate of He could be evaluated by applying implanter foil coatings on pressurized tubes.

Other Applications of the Implanter Foil Approach

He Implantation in SiC

As noted previously, the implanter foil approach can be applied to virtually any material based on any of the available large (n,α) reaction cross section isotopes. For example, we have designed a NiAl implanter approach to study the effects of the He/dpa ratio in SiC specimens to be irradiated in the unshielded HFIR RB* 18J capsule (as part of the US-Japan collaboration JUPITER-II program). The He production is based on the unshielded RB* spectral averaged cross sections for the ^{58}Ni(n, γ), ^{59}Ni(n,α), and ^{59}Ni(n,tot.) reactions [9]. The 4.76 MeV α-particle from ^{59}Ni (n,α) reaction has a range of 14.8 μm in SiC for a typical density 3.21 g/cm^3. A t_f = 6 μm NiAl coating produces a uniform concentration of ≈ 21 appm He/dpa in an ≈ 7 μm thick region, as is shown in Fig. 7a along with the corresponding He uniform concentrations for other implanter foil thickness. Figure 7b shows the increase of the He/dpa ratio in the uniformly deposited region for t_f = 6 □m as function of dpa. We have prepared 6 TEM discs with 6 μm NiAl implanter foil coatings for irradiation in the HFIR 18J experiment that focuses on irradiation effects in SiC at temperatures from 800 to 1300°C and doses up to 5 dpa. The dpa is based on a recently reported Hf shielded RB* spectral averaged dpa cross-section [10].

The 21 appm He/dpa is lower than that produced in a fusion neutron spectra of 50 to 150 appm He/dpa. There are various ways to increase the He/dpa ratio further including: a) use of isotope sources for (n,a) reactions with a larger cross sections (B and Li); b) use of thicker coatings resulting in a smaller region of uniform He deposition (a uniform concentration of ≈ 35 appm He/dpa in a ≈ 2μm region can be produced at 5 dpa using a t_f = 9.9 μm coating); c) use of coatings with higher Ni content (pure Ni would produce 58

appm He/dpa in the 2 μm region cited above); using coatings enriched in ^{58}Ni (pure ^{58}Ni coatings would produce ≈ 85 appm He/dpa in the 2 μm region; or, in principle, ≈ 170 appm He/dpa using Ni pre-irradiated to breed a maximum concentration of ^{59}Ni (3), although this is probably not practical).

Other, and perhaps simpler, implanter design approaches to increasing the He/dpa ratio will be described in a future report. These include micromachining (e.g., by FIBing) multi-dimensionally thin specimens that are effectively implanted in 2 or 3 rather than 1 direction. Further, we will describe a 3-dimensional implantation scheme based on phase-blended powders of Ni (or B or Li) containing alloys along with powders of the material of interest, such as SiC.

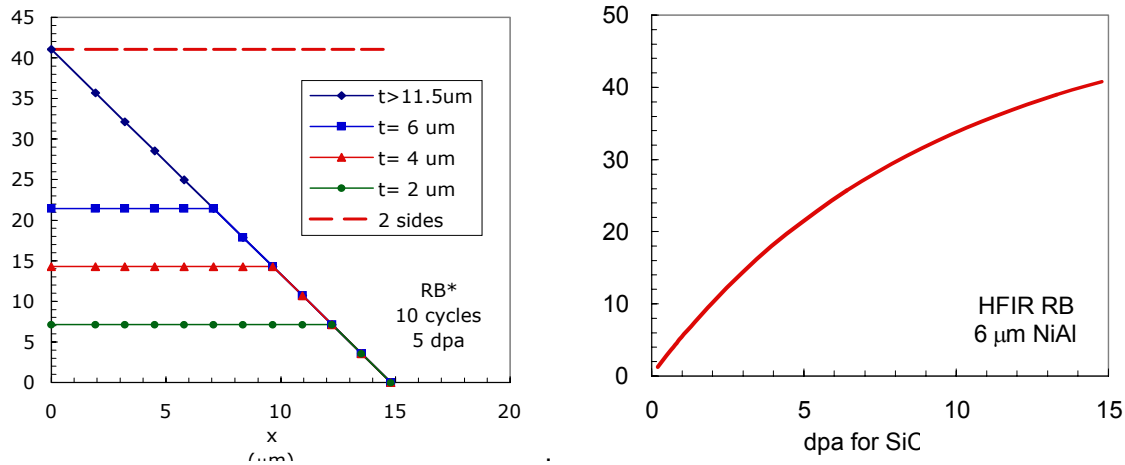

Fig. 7. (a) He implantation profile in SiC irradiated to 5 dpa (10 cycles) in an unshielded RB capsule produced by NiAl coatings with various t_f and (b) the He/dpa ratio as function of dpa for t_f = 6 μm.

Evaluating He Injected into a Blanket Structure from Liquid Li Breeder

While He implantation is a useful experimental technique, it also occurs in blanket fusion first wall and blanket structures in contact with Li-bearing coolants and breeder materials, due to the ^{6}Li (n,t)^{4}He reaction, producing a 2.02MeV α-particle. For example, in the case of liquid Li cooled V alloy blanket, this reaction implants He into and/or through the electrically insulating coatings, needed to reduce MHD pressure drops [11]. For thin coatings, He is also implanted into the V-alloy substrate. The implantation profile for the coating, substrate, and the interface has been estimated for the case of NET (Next European Torus) based on the neutronics and tritium production calculations of Fischer [12]. Two candidate coating materials, CaO and AlN, with thickness ranging from 1 μm to the α-particle range were considered. Because the Li is thick, the He profiles decrease linearly in both the coating and vanadium alloy. Thus the profiles can be easily by determining the residual range in the V-alloy that is not used up in penetrating the coating. This in turn can be determined from the ratio of the ranges in the coating and V-alloy, R_v/R_c, which is approximately constant with the α-particle energy as it slows down as shown in Fig. 8. Ranges of 2.02MeV a-particle in Li, CaO, AlN, and V-4Cr-4Ti from TRIM 2002 code are 22.5, 5.29, 4.83, and 3.42 μm, respectively. Thus, the R_c/R_v ratio is ≈ 1.55 and 1.38 for the CaO and AlN coatings, respectively. The residual range in the vanadium alloy for a coating of thickness t_c is given by $R_v(1 - t_cR_c/R_v)$ for $t_c < R_c$. Thus, for example, an 1 μm coating of CaO reduces the maximum α-range in the V-alloy by ≈ 1.55 μm. The dpa are for the base V-alloy. The He (or He/dpa ratio) profiles are not continuous at the interface due to the difference in the ranges, as well as atom densities when the concentrations, c_{He}, are expressed in terms of atomic fractions (appm).

Figures 9a and b show the He profiles for CaO and AlN coatings, respectively, for a natural lithium coolant. For the coatings with t_c = 2 μm concentration of He exceeds 1000 appm/dpa at the interface,

decreasing to 300 to 500 appm/dpa when t_c = 4 μm. Accumulation of high concentrations of He at the interface and in the coating may induce serious damage, like spalling. This analysis did not consider the co-injection of T, which may not only segregate to and weaken the V-alloy/coating interface, but also contributes additional ^{3}He due to β-decay of T.

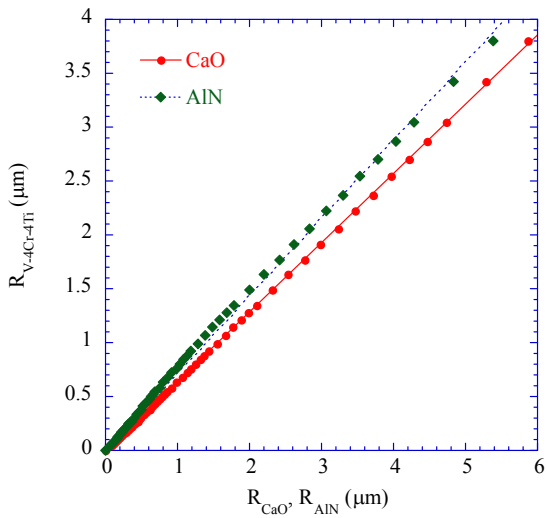

Fig. 8. The relative residual ranges of α-particle in insulator coatings and a V-alloy.

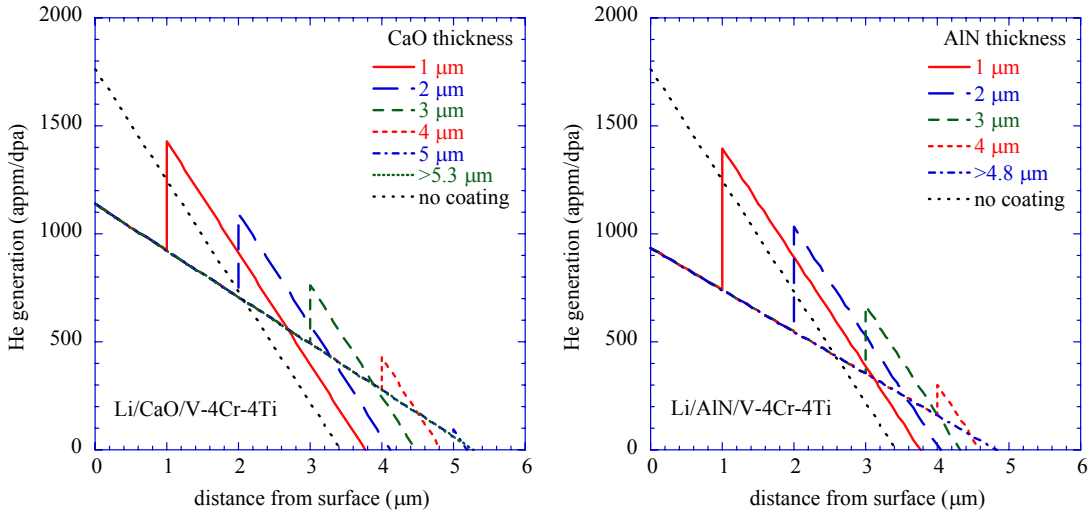

Fig. 9. Profile of He implanted to the blanket structure surface with various thickness of CaO or AlN insulator coating for a liquid Li breeder blanket design.

Discussion and **Summary**

In closing it is useful to note several limitations of the NiAl implanter foil technique. First, if elemental Ni is used the He/dpa ratio is not constant and, as noted previously, increases with dose. Second, the region of implantation is thin and proximate to an interface. This may be significant if the corresponding scales of the grain, precipitate, and dislocation structures are larger than the deposited region. Third, direct

mechanical characterization is confined to low load hardness measurements. Note all of these limitations can be to some extent mitigated using other in situ implanter approaches.

Nevertheless, the in-situ NiAl He implanter foil technique, utilizing ^{59}Ni(n,α) reactions to produce a controlled range of high He/dpa ratios at fusion relevant conditions (dpa, dpa rates, and temperatures), is a powerful new tool for understanding He effects and He-dpa synergisms for fusion relevant conditions. The techniques have been developed and implemented in the HFIR JP26, JP27, and 28/29 irradiation experiments. These irradiations span He/dpa ratios of ≈ 5 to 40 appm He/dpa, doses from 4 to 60 dpa, and temperatures from 300 to 500°C. The experiments involve three classes of materials, with a very wide range of microstructures. The broad array of information garnered from these experiments will be closely integrated with modeling studies to address the key issue of transport, fate, and consequences of He, as well as He management in alloys with carefully designed microstructures. Other applications of the He implantation models are also described.

Future Work

The JP26 irradiation has been completed and the capsule has been disassembled. TEM discs from the He implanter matrix are being prepared for microstructural examination at PNNL and ORNL. Both microhardness and TEM studies on MA957, focusing on issues of He management, and F82H focusing on He transport and fate, will be carried out during the current reporting period. Other implanter and specimen design approaches, including 3-dimensional implantation in phase-blended powders and use of other isotope sources of (n,α) reactions (B or Li), will also be developed.

Acknowledgements

This research was supported by the DOE Office of Fusion Energy Science (Grant # DE-FG03-94ER54275). The authors are grateful to Mr. D. Klingensmith, Dr. M. Alinger, Mr. D. Stave, Dr. H. Kishimoto (UCSB), and Dr. R. Stoller (ORNL) for outstanding technical support.

References

1. N. H. Packan and W. A. Coghlan, Nucl. Technol. 40 (1978) 208.
2. F. A. Garner, Radiat. Eff. 66 (1982) 211.
3. G. R. Odette, J. Nucl. Mater. 141–143 (1986) 1011.
4. L. K. Mansur and W. A. Coghlan, ASTM STP 1046 (1989) 315.
5. H. Matsui, K. Nakai, A. Kimura, T. Shikama, M. Narui, and H. Kayano, J. Nucl. Mater. 233–237 (1996) 1561.
6. L. R. Greenwood, F. A. Garner, B. M. Oliver, M. L. Grossbeck, and W. G. Wolfer, ASTM STP 1447 (2004).
7. G. R. Odette, presented in ICFRM11.
8. G. R. Odette, T. Yamamoto, H. J. Rathbun, M. Y. He, M. L. Hribernik, and J. W. Rensman, J. Nucl. Mater. 323 (2003) 313.
9. T. Yamamoto, G. R. Odette, H. Kishimoto, J. W. Rensman, and P. Miao, Journal of Nuclear Materials (submitted).
10. L. R. Greenwood, D. W. Kneff, R. P. Skowronski, and F. M. Mann, J. Nucl. Mater. 123 (1994) 1002.
11. R. F. Mattas, D. L. Smith, C. B. Reed, J. H. Park, I. R. Kirillov, Yu. S. Strebkov, A. E. Rusanov, and S. N. Votinov, Fusion Eng. Des. 39–40 (1998) 659.
12. U. Fischer, Fusion Technol. 22 (1992) 251.